

Fabrication of Cu-Doped CeO₂ Catalysts with Different Dimension Pore Structures for CO Catalytic Oxidation

Yunfei Su^{1,2} · Lingfeng Dai^{1,2} · Qingwen Zhang^{1,2} · Yunzhen Li^{1,2} · Jiayi Peng³ · Ren'an Wu³ · Weiliang Han⁴ · Zhicheng Tang⁴ · Yi Wang^{1,2}

Published online: 3 November 2016
© Springer Science+Business Media New York 2016

Abstract Transition metal oxides (TMOs) applied as catalysts whose catalytic activities are directly affected by their pores size and pores distributions. Herein, two-dimensional Cu-doped CeO₂ (2D@Cu–CeO₂) and three-dimensional Cu-doped CeO₂ (3D@Cu–CeO₂) were prepared by adopting the mesoporous silica SBA-15 and KIT-6 as templates, respectively. Nanometer Cu-doped CeO₂ (nano@Cu–CeO₂) was synthesized by the method of precipitation. All catalysts were evaluated for the catalytic oxidation of CO, and the 3D@Cu–CeO₂ catalyst exhibited the highest catalytic activity (complete conversion temperature T₁₀₀=50 °C), which can be ascribed to the three-dimensional porous channel structure, larger specific surface area and abundant active surface oxygen species. In addition, complete conversion of CO had remained the same after 3D@Cu–CeO₂ was observed for 12 h, indicating it has the best catalytic stability for CO.

Keywords Different dimension · CO catalytic oxidation · Nanocasting route · Cu-doped CeO₂ catalyst

✉ Ren'an Wu
wurenan@dicp.ac.cn

✉ Yi Wang
wangyi@wibe.ac.cn

- ¹ Institute of Biomaterials and Engineering, Wenzhou Medical University, Wenzhou 325000, China
- ² Wenzhou Institute of Biomaterials and Engineering, Chinese Academy of Sciences, Wenzhou 325000, China
- ³ CAS Key Lab of Separation Sciences for Analytical Chemistry, Dalian Institute of Chemical Physics, Chinese Academy of Sciences, Dalian 116023, China
- ⁴ National Engineering Research Center for Fine Petrochemical Intermediates, Lanzhou Institute of Chemical Physics, Chinese Academy of Sciences, Lanzhou 730000, China

1 Introduction

Carbon monoxide (CO) is one of the main gaseous pollutants, which is usually emitted from many industrial process, transportation and domestic activities. Carbon monoxide of low concentration is harmful to human health and environment. It was confirmed that the CO could lead to the lack of oxygen in the body, result in life-threatening. Therefore, it is essential to remove the CO, and catalytic oxidation method is an efficient way [1–4]. Also, the CO oxidation reaction constitutes a prime example of a non-equilibrium system that exhibits a rich variety of behavioral patterns and complex irreversible critical behaviors [5, 6]. Hence, the catalytic oxidation of CO has attracted much attention in the past decade.

As one of the transition metal oxides (TMOs), ceria has been widely applied for the effective CO catalytic oxidation because of its unique properties, such as unique redox property and high oxygen storage capacity [7, 8]. To enhance ceria catalytic activity, generally, one may either optimize its morphologies/structure or combine it with secondary species, for examples, noble metals or other metal oxides, to form composites [9–18]. In the first strategy, ceria with different morphologies/structure have been designed and studied [11, 15, 19–21]. Especially, the pore structure with high surface area, which was directly affect their performance in catalytic oxidation [22]. In the second strategy, in spite of ceria-based with noble metal catalyst exhibited high performance for CO catalytic oxidation at low temperature, the applications of precious metal catalysts are limited due to their high cost and low thermal stability. Compared with noble metal-based catalysts, due to the synergistic effect, the ceria-based bimetal oxides by combining ceria with other cheap TMOs also exhibited remarkable catalytic activity in CO oxidation reaction. Therefore,

the construction of ceria-based bimetal oxides with open pore structures could take full advantages of two strategies stated above, and thus is of particular interest to optimize their catalytic activities.

Among ceria-based bimetal oxides, copper–ceria catalysts exhibit an excellent catalytic activity for CO oxidation, and they have been found to be good candidates as cheap and efficient catalysts, especially in CO catalytic oxidation [23–26]. Yen et al. [23] prepared mesostructured copper/ceria catalysts by adopting the mesoporous silica MCM-48 for catalytic oxidation of CO at low temperature. The results showed that the reducibility and catalytic performance were influenced by structural parameters such as pore size and pore structure. CuO–CeO₂ nanorod with mesoporous structure were synthesized by a facile and mild strategy [24]. The mesoporous CuO–CeO₂ nanorod catalysts exhibited high CO catalytic activity, and was observed without obvious loss in activity even after thermal treatment at a high temperature of 500 °C. The results were due to mesoporous structure of CuO–CeO₂ nanorod catalyst. Wei et al. prepared nanoporous CuO–CeO₂ composite catalysts by a facile technique. The porous CuO–CeO₂ composite catalysts exhibited enhanced activity for CO catalytic oxidation [25]. In the literature, the pore structure of catalyst had a crucial influence on the catalytic performance for low temperature CO catalytic oxidation.

Therefore, it is meaningful and significant to study the effects of Cu-doped CeO₂ catalysts with the same components but different pore structures to the CO oxidation and investigate whether the three-dimensional (3D) porous channels of Cu-doped CeO₂ can improve the catalytic activity at low temperature. Herein, different structure of catalysts including nanometer (nano) Cu-doped CeO₂, two-dimensional (2D) Cu-doped CeO₂ and three-dimensional (3D) Cu-doped CeO₂ were synthesized. Their structure and catalytic activity for CO oxidation were investigated.

2 Experimental

2.1 Preparation of Mesoporous KIT-6 and SBA-15 Silica

Three-dimensional mesoporous silica KIT-6 was synthesized according to the previously reported method [27]. Typically, 6.0 g P123 (EO20PO70EO20, MW=5800, Aldrich) was dissolved in 144 g distilled water and 12 g 35 wt% HCl solution with stirring at 30 °C. After complete dissolution, 6.0 g BuOH was added into above solution at once. Then, 12.86 g TEOS was added to the homogeneous clear solution. This mixture was left under vigorous and constant stirring at 30 °C for 24 h. Subsequently, the solution was transferred to a Teflon-lined stainless steel

autoclave at 100 °C for 24 h. The sample was dried at 100 °C and calcined at 550 °C for 5 h to completely eliminate the template. The resulting powder was three-dimensional mesoporous silica KIT-6.

Two-dimensional mesoporous silica SBA-15 was synthesized according to the previously reported method [28]. In a typical synthesis, 4.0 g P123 (EO20PO70EO20, MW=5800, Aldrich) was dissolved in 120 ml distilled water and 20 ml 35 wt% HCl solution with stirring at 30 °C. After complete dissolution, 9.0 g TEOS was added to the homogeneous clear solution. This mixture was left under vigorous and constant stirring at 30 °C for 24 h. Then, the solution was transferred into a Teflon-lined stainless steel autoclave at 100 °C for 24 h. The sample was dried at 100 °C and calcined at 550 °C for 5 h to completely eliminate the template. The white mesoporous SBA-15 powder was obtained.

2.2 Synthesis of Mesoporous 3D@Cu–CeO₂ and 2D@Cu–CeO₂

The three-dimensional(3D) Cu-doped CeO₂ catalyst with Cu/(Cu+Ce) atomic ratios are 20%, denoted as 3D@Cu–CeO₂. Typically, 2.5 g Ce(NO₃)₃·6H₂O and 0.43 g Cu(NO₃)₂·3H₂O were dissolved in 15 ml ethanol by stirring at room temperature. After complete dissolution, 1 g mesoporous silica template (KIT-6) was added. The mixture was stirred at room temperature until a nearly dry powder was obtained. The sample was then heated slowly to 200 °C and calcined at the same temperature for 5 h to pyrolyze the nitrate. The result material was impregnated again with 15 ml of ethanol containing 1.95 g Ce(NO₃)₃·6H₂O and 0.32 g Cu(NO₃)₂·3H₂O, followed by calcination at 500 °C for 5 h with a ramp 1 °C min⁻¹ for formed metal oxide. The sample was twice treated with a hot 2 M NaOH solution to remove the silica template, followed by washing with water and ethanol for two times, and then dried at 100 °C overnight. Two-dimensional (2D) Cu-doped CeO₂ (denoted as 2D@Cu–CeO₂) was prepared by the similar method (only changed 3D KIT-6 into 2D SBA-15).

2.3 Synthesis of Nano@Cu–CeO₂

Nanometer (nano) Cu-doped CeO₂ (Cu/(Cu+Ce) atomic ratios are 20%) was prepared by the precipitation method [29]. 2.6 g Ce(NO₃)₃·6H₂O and 0.29 g Cu(NO₃)₂·3H₂O were added into 20 ml distilled water under stirring at room temperature. After complete dissolution, the pH value of the solution was adjusted to 9.5 with 1 M NaCO₃ solution. The solution was continually stirred for 10 h. The precipitate was filtrated, washed and dried at 100 °C and calcined at 500 °C for 5 h to obtain nanometer (nano) Cu-doped CeO₂ (denoted as nano@Cu–CeO₂).

2.4 Catalyst Characterization

Powder X-ray diffraction (XRD) analysis was performed to verify the crystallographic phase present Cu–CeO₂ catalysts. XRD patterns of the samples were recorded on a Rigaku D/MAX-RB X-ray diffractometer with a target of Cu K α operated at 60 kV and 55 mA with a scanning speed of 5° min⁻¹. The 2 θ of wide-angle ranged from 20° to 80° and the 2 θ of low-angle ranged from 0.6° to 5°.

Transmission electron microscopy (TEM) experiments were measured on a JEOL JEM-2010 transmission electron microscope equipped with an Oxford energy-dispersive X-ray (EDX) spectrometer attachment operating at 200 kV.

The specific surface area and the mean pore diameter of the catalysts were determined by nitrogen adsorption in accordance with the BET method, measured on Micromeritics ASAP 2010 instrument. The BET surface area were determined based on six measurements at relative pressures of N₂ in the range of 0.05–1.00.

Fourier transform infrared spectroscope (FTIR, Nexus 870FT-IR) was used to record the FTIR spectra of the sample ranging from 400 to 4000 cm⁻¹.

Chemical states of the atoms in the catalyst surface were investigated by X-ray photoelectron spectroscopy (XPS) on a VG ESCALAB 210 Electron Spectrometer (Mg K α radiation; $h\nu = 1253.6$ eV). XPS data were calibrated using by the binding energy of C1s (284.6 eV) as the standard.

The O₂-TPD was test on a chemisorb 2720 TPX. The catalysts were treated at 30°C in a 5% O₂/He mixture with a flow rate of 50 ml min⁻¹. The catalysts adsorbed enough O₂ when the treatment temperature decreased below 50°C, at which point the carrier gas was changed to pure He. The temperature was increased to 800°C at a rate of 10°C min⁻¹.

2.5 Measurements of Catalytic Performance

Catalytic activity tests were performed in a continuous-flow fixed-bed microreactor. A glass tube with an inner diameter of 6 mm was used as the reactor tube. About 300 mg catalyst with the average diameter of 20–40 mesh was placed into the tube. The reaction gas mixture consisted of 1 vol.% CO balanced with air was passed through the catalyst bed at a total flow rate of 50 ml min⁻¹. A typical weight hourly space velocity (WHSV) was 10,000 ml g⁻¹ h⁻¹. The composition of the influent and effluent gas was detected with an online GC-7890II gas chromatograph equipped with a thermal conductivity detector. As we all known, CO oxidation reaction is accompanied by a reduction in the number of moles. In this paper, this change of moles was neglected. Therefore, the CO conversion was calculated based on the outlet CO:

$$\text{Conversion of CO\%} = \frac{([\text{CO}]_{\text{in}} - [\text{CO}]_{\text{out}})}{[\text{CO}]_{\text{in}}} \times 100$$

The [CO]_{in} and [CO]_{out} was CO concentration (vol%) in mixture gas before and after CO catalytic oxidation reaction, respectively.

3 Results and Discussion

3.1 Structure Characterization of Catalysts

The wide-angle XRD patterns of the Cu–CeO₂ catalysts were displayed in Fig. 1A. From the XRD patterns, the absence of CuO diffraction peaks for all catalysts, and the result was ascribed to the substitution of copper in the ceria lattice or the formation of extremely small copper oxide clusters, indicating homogeneous dispersion of copper species on the ceria matrices [30]. As we known, the better doped metal copper dispersion, the more it contributed to improve the catalytic activity. Compared with

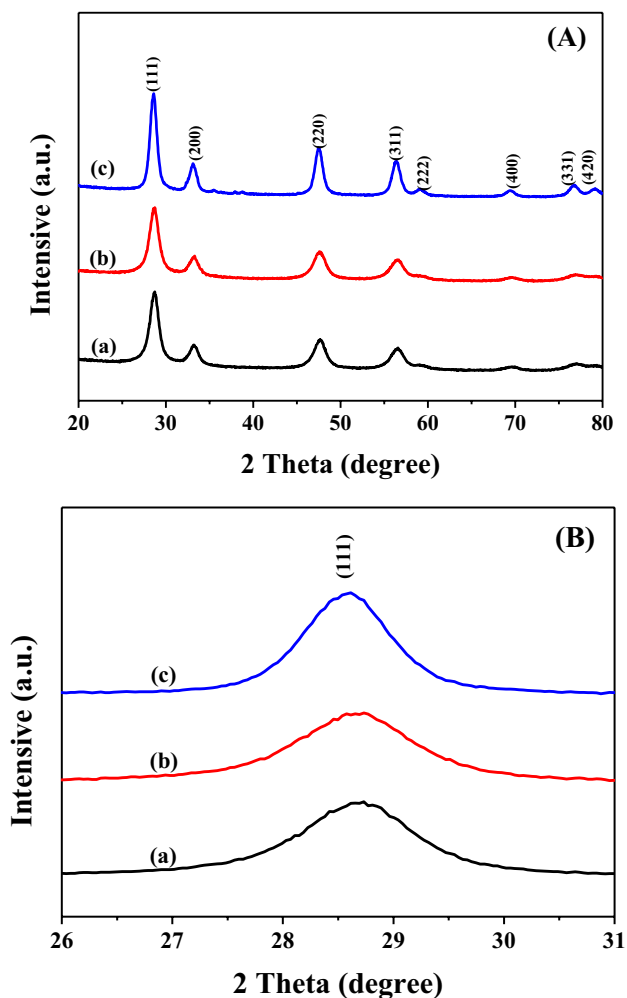


Fig. 1 Wide-angle A XRD patterns of a 3D@Cu–CeO₂, b 2D@Cu–CeO₂ and c nano@Cu–CeO₂, B is a magnification of ceria (111) plane

the XRD patterns of the standard CeO₂ sample (JCPDS PDF#43-1002), 3D@Cu–CeO₂, 2D@Cu–CeO₂ and nano@Cu–CeO₂ all showed a typical crystalline fluorite structure with eight characteristic diffraction peaks corresponding to (111), (200), (220), (311), (222), (400), (331) and (420) planes, respectively. The average size of crystalline catalyst was calculated from the ceria (111) plane using Scherrer's formula, and the results was showed in Table 1. It was seen that the particle size sequence was nano@Cu–CeO₂ (11.7 nm) > 2D@Cu–CeO₂ (7.36 nm) > 3D@Cu–CeO₂ (6.38 nm). 3D@Cu–CeO₂ showed relatively smaller average particle size compared with 2D@Cu–CeO₂ and nano@Cu–CeO₂. The small size of particles would provide high amount of reactive edge sites, which was conducive to improve catalytic activity.

The pore structures of mesoporous 3D@Cu–CeO₂ and 2D@Cu–CeO₂ were examined by N₂ adsorption–desorption measurements. As presented in Fig. 2, it was shown that 3D@Cu–CeO₂ and 2D@Cu–CeO₂ exhibited the hysteresis phenomenon belong to the type IV isotherms, which was in good agreement with many other previously mesoporous transition metal oxides synthesized by the hard templated route [31, 32]. The hysteresis ring of 3D@Cu–CeO₂ catalyst was bigger than 2D@Cu–CeO₂ catalyst. The reason was that 3D@Cu–CeO₂ and 2D@Cu–CeO₂ have different porous channel structures [23]. The BET surface areas of 2D@Cu–CeO₂ catalyst was smaller than that of 3D@Cu–CeO₂ catalyst. The pore size distributions was calculated from the desorption isotherms by the BJH method are shown in Fig. 2, inset. It was seen that the catalysts peaks were at pore size of 3.2 and 5 nm for 2D@Cu–CeO₂ and 3D@Cu–CeO₂, respectively. The result showed that 2D@Cu–CeO₂ and 3D@Cu–CeO₂ are a perfect replica structure of their templates. The pore structural parameters from N₂ adsorption–desorption measurements were summarized in Table 1. From the Table 1, it clearly showed that the BET surface areas of 2D@Cu–CeO₂ and 3D@Cu–CeO₂ were larger than nano@Cu–CeO₂ (31.9 m² g⁻¹)

Table 1 Pore structure parameters and particle size of the prepared catalysts

Catalysts	BET surface area (m ² g ⁻¹)	Average pore diameter (nm)	Pore volume (cm ³ g ⁻¹)	D _{CeO₂} ^a (nm)
3D@Cu–CeO ₂	151.8	5.0	0.36	6.38
2D@Cu–CeO ₂	120.6	3.2	0.32	7.36
Nano@Cu–CeO ₂	31.9	–	–	11.7

^aCalculated the average size of crystalline CeO₂ from line broadening of the ceria (111) plane using Scherrer's formula

catalyst. Especially, the BET surface areas of 3D@Cu–CeO₂ reached 151.8 m² g⁻¹.

The morphology of the three catalysts are investigated by TEM as shown in Fig. 3a–c. From the Fig. 3, no obvious nonporous particles are observed in the TEM images, indicating almost all the metal nitrate were successfully filled inside the mesopores and transformed in situ to the fluorite during the calcination. The 3D@Cu–CeO₂ and 2D@Cu–CeO₂ catalysts exhibited the ordered three-dimensional and two-dimensional mesoporous structure, and retained the

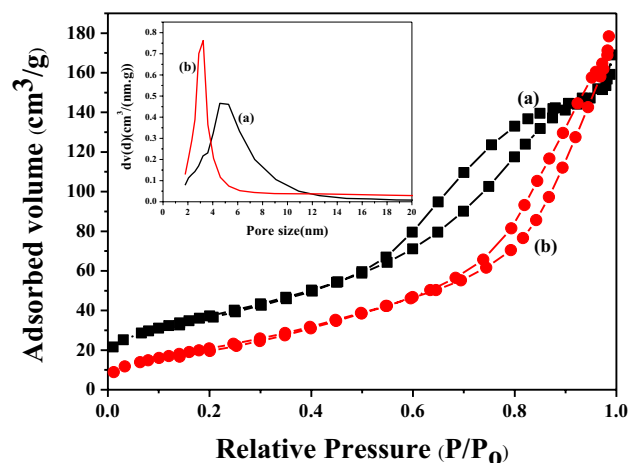


Fig. 2 N₂ adsorption–desorption isotherms of a 3D@Cu–CeO₂ and b 2D@Cu–CeO₂. The inset is BJH pore size distributions

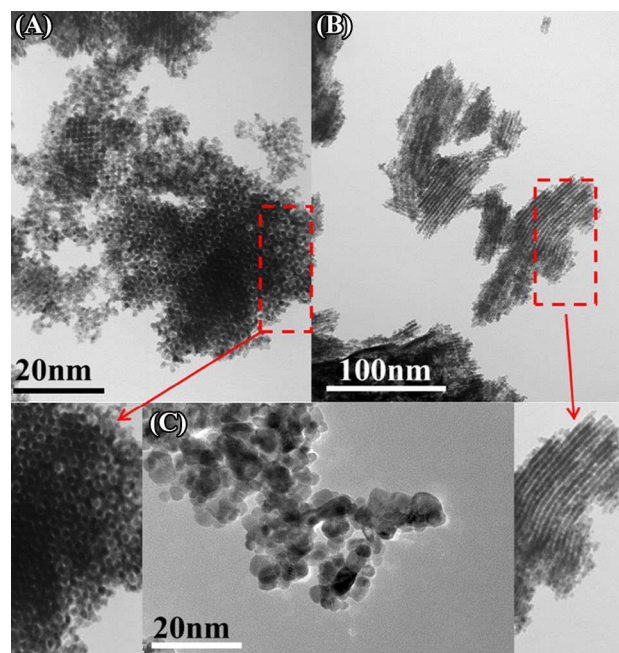


Fig. 3 TEM images of a 3D@Cu–CeO₂, b 2D@Cu–CeO₂ and c nano@Cu–CeO₂

ordered structure of the KIT-6 and SBA-15, respectively. The nano@Cu–CeO₂ catalyst is composed of polycrystalline without pores. The results are consistent with the BET analysis.

3.2 FTIR Analysis

To confirm whether the mesoporous silica template had been completely removed, the catalyst was characterized by FTIR (Fig. 4). For hard template KIT-6 and SBA-15, the peaks centered at 1086, 810 and 465 cm⁻¹ may be assigned to Si–O–Si asymmetrical stretching vibration, symmetrical stretching vibration and bending vibration, respectively [13]. The peak centered at 960 cm⁻¹ was related to Si–OH stretching vibration [16]. For 3D@Cu–CeO₂ and 2D@Cu–CeO₂ catalysts, the peak centered at 513 cm⁻¹ was originated from Cu–O bending vibration [33]. The peaks centered at 838, 1006 and 1377 cm⁻¹ were related to CeO₂ structure [34]. For all the samples, the broad absorption peaks centered at 1630 and 3420 cm⁻¹ were associated with the hydroxyl groups of the superficial adsorbed or crystallized water. By comparing the mesoporous silica template with the corresponding catalysts (KIT-6 and 3D@Cu–CeO₂, SBA-15 and 2D@Cu–CeO₂), the absence of the characteristic absorption peaks from the template or the catalysts, indicates that the mesoporous silica template had been completely removed from catalysts.

3.3 Surface Active Oxygen Species of Different Catalysts

XPS analysis was further conducted to gain the binding energy and the features of chemical species located in the

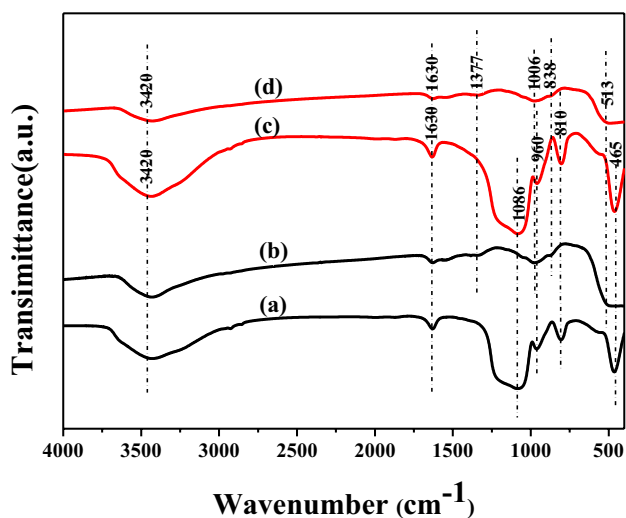


Fig. 4 FTIR spectra of *a* KIT-6, *b* 3D@Cu–CeO₂, *c* SBA-15 and *d* 2D@Cu–CeO₂

surface of different catalysts. Figure 5A shows the Ce 3d spectra of the 3D@Cu–CeO₂, 2D@Cu–CeO₂ and nano@Cu–CeO₂ catalysts. It can be seen that the different catalysts have a rather complex structure. The fitting process was referred to the literature [35], they (V_1 – V_3 , V_4 , V_6 , V_7) were characteristic of Ce⁴⁺ 3d final states and they (V_0 , V_1 , V_5) were characteristic of Ce³⁺ 3d final states. The results showed that the coexistence of Ce³⁺ and Ce⁴⁺ species on the surface of different Cu–CeO₂ catalysts. It was reported that there were Ce³⁺ ions in the ceria, indicating the forming of an oxygen vacancy in order to maintain electrostatic equilibrium. The Ce³⁺ percentages were calculated in Table 2, which was shown that the percentage of Ce³⁺ in 3D@Cu–CeO₂ (27%) catalyst were higher than those of 2D@Cu–CeO₂ (21%) and nano@Cu–CeO₂ (13%) catalysts. In addition, the result implied more oxygen vacancies on the surface of 3D@Cu–CeO₂ catalyst, due to its three-dimensional channel structure which provides

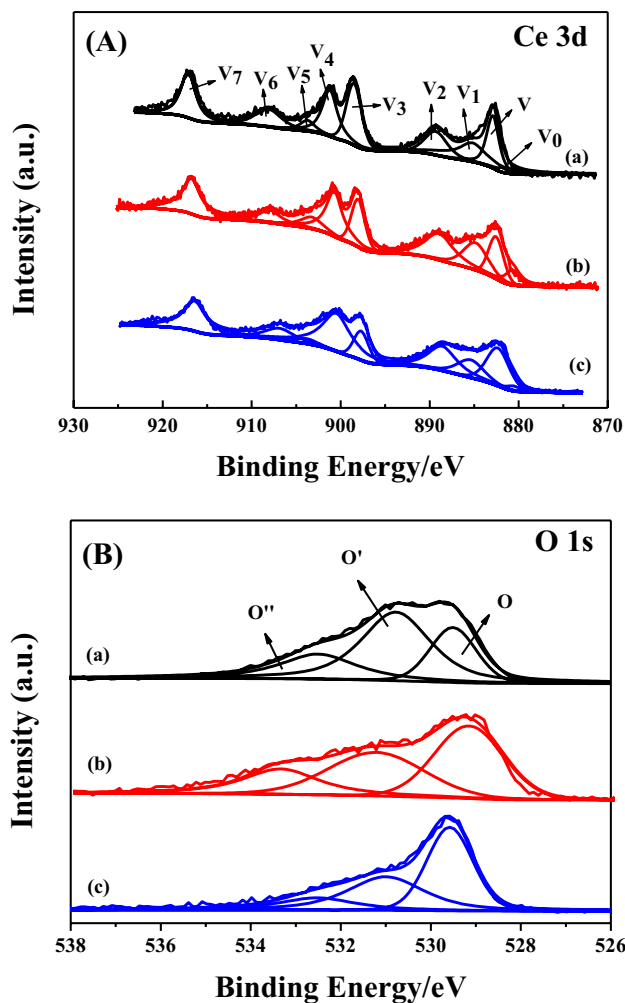


Fig. 5 **A** Ce 3d and **B** O 1s XPS spectra of *a* 3D@Cu–CeO₂, *b* 2D@Cu–CeO₂ and *c* nano@Cu–CeO₂

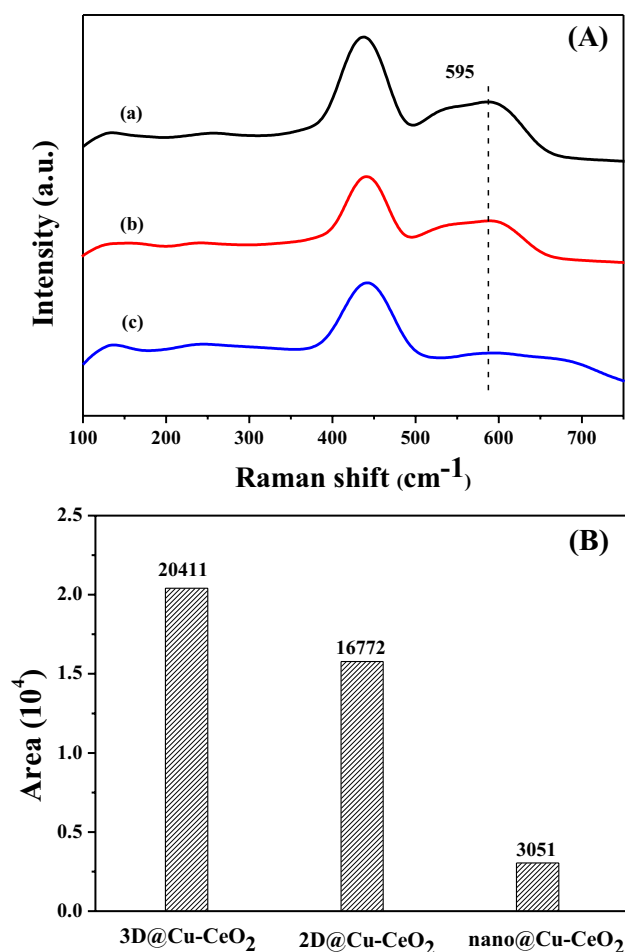
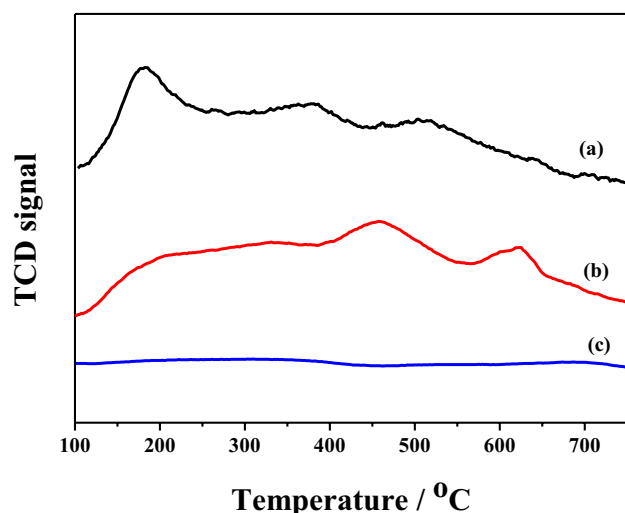
Table 2 The XPS data for all catalysts

Catalysts	Ce ³⁺ /(Ce ³⁺ +Ce ⁴⁺)	O'/(O+O'+O'')
3D@Cu–CeO ₂	0.27	0.54
2D@Cu–CeO ₂	0.21	0.46
nano@Cu–CeO ₂	0.13	0.39

higher surface area for oxygen vacancies. Figure 5B was the O 1s spectra of the 3D@Cu–CeO₂, 2D@Cu–CeO₂ and nano@Cu–CeO₂ catalysts. Three kinds of peaks (O, O', O'') can be identified by the deconvolution of the O1s spectra. The one (O) with lower binding energy was assigned to lattice oxygen in the metal oxides, while (O') was corresponding to the chemisorbed oxygen or/and weakly bonded oxygen species, and (O'') with the highest binding energy was the surface oxygen in a formate of hydroxyl species and/or adsorbed water species on the surface [36]. The percentages of O' (active chemisorbed oxygen) for different catalysts were listed in Table 2. The table showed that the 3D@Cu–CeO₂ (54%) possesses highest amount of O', as compared with that of 2D@Cu–CeO₂ (46%) and nano@Cu–CeO₂ (39%). Overall, 3D@Cu–CeO₂ has a wealth of surface active chemisorbed oxygen and oxygen vacancies, which play an important role in CO catalytic oxidation.

In order to investigate the oxygen vacancy and Cu distribution, all catalysts were analyzed by Raman measurement, as displayed in Fig. 6A. It can be observed that all three catalysts exhibited the characteristic peaks at around 453 and 595 cm⁻¹. Pure CeO₂ with fluorite-structure has a Raman peak at 465 cm⁻¹ as reported in our previous work [2]. By comparing with pure CeO₂, once copper introduced, the peak shifts from 465 to 453 cm⁻¹, with peak broader and weaker for all catalysts in this work. The reason of shifting and broadening may be the presence of oxygen vacancies, which is related to structural defects derived from partially incorporation of copper species into CeO₂ [37]. The peak center at 595 cm⁻¹ was ascribed to oxygen vacancy. Moreover, the amount of oxygen vacancy over different catalysts were calculated by Gaussian deconvolution at the region around 595 cm⁻¹ [38], as shown in Fig. 6B. It can be seen that the 3D@Cu–CeO₂ possesses highest oxygen vacancy concentration (about seven times higher than that of nano@Cu–CeO₂). The result was mainly due to the 3D structure of 3D@Cu–CeO₂ catalyst. The oxygen vacancy was beneficial for oxygen in the gas phase to be activated, thus promotes the CO oxidation reaction.

The O₂ temperature programmed desorption (O₂-TPD) patterns of 3D@Cu–CeO₂, 2D@Cu–CeO₂ and nano@Cu–CeO₂ catalysts are shown in Fig. 7. The oxygen species were desorbed from easiest to hardest as follows: oxygen molecule (O₂) > oxygen molecule anion (O₂⁻) > oxygen anion (O⁻) > lattice oxygen (O²⁻). O₂⁻ was molecule

**Fig. 6** A Raman spectra of a 3D@Cu–CeO₂, b 2D@Cu–CeO₂ and c nano@Cu–CeO₂, B integrated peak areas at 595 cm⁻¹ for all catalysts**Fig. 7** O₂-TPD patterns of a 3D@Cu–CeO₂, b 2D@Cu–CeO₂ and c nano@Cu–CeO₂

adsorption oxygen, and O⁻ was surface chemical adsorption oxygen. O₂⁻ and O⁻ belong to surface active oxygen species, which were easy to desorb from the metal oxide. The lattice oxygen was extremely hard to desorb from the metal oxide [39, 40]. From the Fig. 7, it can be seen that there were three peaks of oxygen desorption appearing at 180, 380 and 540 °C for 3D@Cu–CeO₂ catalyst, and two peaks at 460 and 640 °C for 2D@Cu–CeO₂ catalyst. According to previous reported [33], these desorption peaks were belong to the surface active oxygen. However, the nano@Cu–CeO₂ catalyst had almost no active oxygen. In contrast to 3D@Cu–CeO₂ and 2D@Cu–CeO₂, there was no peak at 180 °C for 2D@Cu–CeO₂, and the desorption peaks were relatively weak. The results indicated that the 3D@Cu–CeO₂ surface has abundant surface active oxygen species (O₂⁻ and O⁻). The phenomenon should be attributed to 3D mesoporous structure of 3D@Cu–CeO₂, which provides more lattice defect and oxygen vacancy. It was better for oxygen in the gas phase to be activated and adsorbed onto the solid surface. The studies have revealed that the surface active oxygen can easily participate in the catalytic oxidation reaction and thus enhance the catalytic activity.

3.4 Catalytic Activity

The Fig. 8 showed the catalytic performance of 3D@Cu–CeO₂, 2D@Cu–CeO₂ and nano@Cu–CeO₂ catalysts for the oxidation of CO. From the figure, 3D@Cu–CeO₂ and 2D@Cu–CeO₂ exhibited a similar catalytic behavior that the CO oxidation activity increased with the catalytic reaction

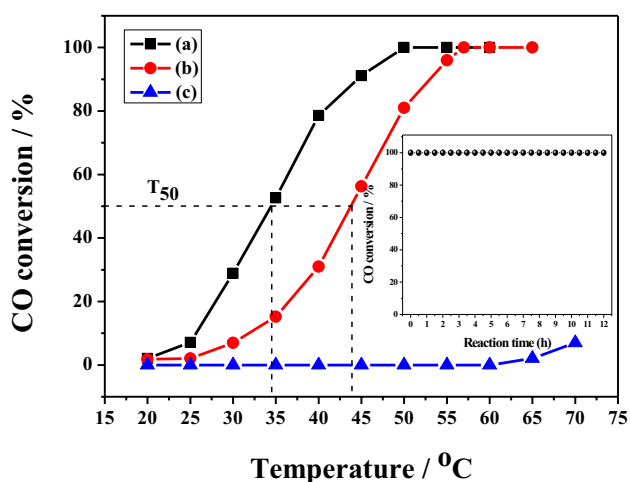


Fig. 8 Catalytic activity of a 3D@Cu–CeO₂, b 2D@Cu–CeO₂ and c nano@Cu–CeO₂ catalysts for CO oxidation, the inset is the stability diagram of 3D@Cu–CeO₂ catalyst. Reaction conditions: under 1% CO balance air, WHSV = 10,000 ml h⁻¹ g⁻¹

temperature. And the T₁₀₀ (the temperature when the conversion was 100%) of 3D@Cu–CeO₂ and 2.

D@Cu–CeO₂ were 50 and 57 °C, and the T₅₀ (the temperature when the conversion was 50%) were only 34 and 44 °C respectively. However, the nano@Cu–CeO₂ showed negligible catalytic activity at ≤60 °C and presents CO conversion of 3% at 65 °C. Generally speaking, the activity of a metal catalyst with same component was influenced by surface area, pore structure and surface oxygen species. In these factors, the most fundamental reason for distinct CO catalytic activity was that the catalysts have a different pore structure. Because the pore structure can directly influence the surface area and the surface oxygen species of catalyst. By comparing with nano@Cu–CeO₂ and 2D@Cu–CeO₂, 3D@Cu–CeO₂ possesses high surface area and more active oxygen species, showing the best catalytic activity of CO. The result showed that the 3D mesoporous structure was favorable for the CO catalytic oxidation. The catalytic stability was evaluated over the best catalyst 3D@Cu–CeO₂ in Fig. 8, inset. It was shown that the catalytic activity unchanged after three cycles and no loss of CO conversion is observed after 12 h on stream at 50 °C, indicating the high stability of the catalyst.

The CO catalytic activities of our CuO–CeO₂ catalyst were compared with other reported catalysts with the similar components but different pore structures as presented in Table 3. It can be seen that our 3D@Cu–CeO₂ and 2D@Cu–CeO₂ showed about 2–3 fold lower T₁₀₀ as compared with the reported CuO–CeO₂ catalysts [41, 42]. Therefore, it indicated that 3D pore structure of CuO–CeO₂ can lead to appreciable catalytic activities for CO oxidation.

3.5 Apparent Activation Energy

The kinetics of catalytic oxidation of CO has gained much attention. The Arrhenius plots of 3D@Cu–CeO₂, 2D@Cu–CeO₂ and nano@Cu–CeO₂ for CO oxidation reaction is following:

$$r_{obs} = \frac{F \cdot U_{CO} \cdot X_{CO}}{W_{cat}} \quad (1)$$

where F refers to the total flow of the reaction gas (50 ml min⁻¹), U_{CO} is the CO percentage composition (1 vol.%), W_{cat} is the catalyst weight (0.3 g), and X is the CO conversion (%).

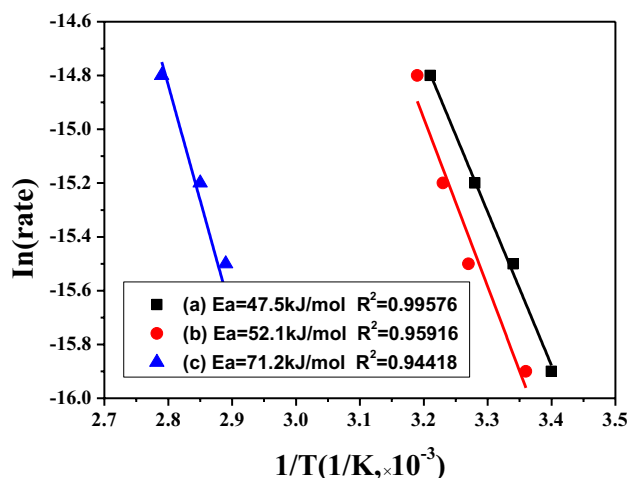
$$r = k_{co} p_{co}^x p_{o_2}^y \quad (2)$$

$$k_{co} = A \exp(-Ea/RT) \quad (3)$$

A is the preexponential factor, R is the ideal gas constant, T is the reaction temperature, p_{co} is the partial pressure of CO, p_{o₂} is the partial pressure of O₂. Taking the logarithm of Eqs. (2, 3) can be obtained.

Table 3 Compared Cu doped CeO₂ catalysts on activity of CO oxidation

Catalysts	Structure	Reaction condition	T ₁₀₀ (°C)	References
CuO–CeO ₂	Nano	SV = 9600 ml g ⁻¹ h ⁻¹ CO = 1 %	130	[41]
CuO–CeO ₂	Disorder-mesoporous	SV = 9600 ml g ⁻¹ h ⁻¹ CO = 1 %	85	[42]
CuO–CeO ₂	Disorder-mesoporous	SV = 16,000 ml g ⁻¹ h ⁻¹ CO = 1 %	125	[43]
CuO–CeO ₂	Order-mesoporous	SV = 30,000 ml g ⁻¹ h ⁻¹ CO = 1 %	145	[44]
3D@C–CeO ₂	3D-Mesoporous	SV = 10,000 ml g ⁻¹ h ⁻¹ CO = 1 %	50	This work
2D@Cu–CeO ₂	2D-Mesoporous	SV = 10,000 ml g ⁻¹ h ⁻¹ CO = 1 %	57	This work

**Fig. 9** Arrhenius plots of $\ln r$ versus $1/T$ for CO oxidation over the *a* 3D@Cu–CeO₂, *b* 2D@Cu–CeO₂ and *c* nano@Cu–CeO₂ catalysts. (R^2 is correlation coefficient)

$$\ln r = -Ea/RT + \ln A + x \ln p_{co} + y \ln p_{o_2} \quad (4)$$

In the process of kinetics data testing, the composition of the reactant gas remained essentially unchanged, therefore, $\ln A$, $\alpha \ln p_{co}$ and $\beta \ln p_{o_2}$ could be regarded as approximately constant, and Eq. (4) can be simplified to $\ln r = -Ea/RT + C$. The activation energy (Ea) can be obtained from the slope of the resulting linear plot of $\ln r$ versus $1/T$.

Figure 9 shows the Arrhenius plots of 3D@Cu–CeO₂, 2D@Cu–CeO₂ and nano@Cu–CeO₂ catalysts at a CO conversion of <25%, respectively. Excellent linear relationships (the correlation coefficients R^2 were close to one) of $\ln r$ versus $1/T$ for all three catalysts were obtained. The measured apparent activation energy Ea were 3D@Cu–CeO₂ (47.5 kJ mol⁻¹) < 2D@Cu–CeO₂ (52.1 kJ mol⁻¹) < nano@Cu–CeO₂ (71.2 kJ mol⁻¹). The discrepancy in Ea value might be due to the differences in pore structure and surface active oxygen species of the

as-prepared catalysts. The lower the Ea value, the easier the complete oxidation of CO, and hence the better is the performance of a catalyst. The Ea of 3D@Cu–CeO₂ were lowest compared with 2D@Cu–CeO₂ and nano@Cu–CeO₂. Therefore, the results of kinetic investigations confirm that the 3D@Cu–CeO₂ catalyst exhibited good catalytic activity for CO catalytic oxidation. The results correspond well with Fig. 8.

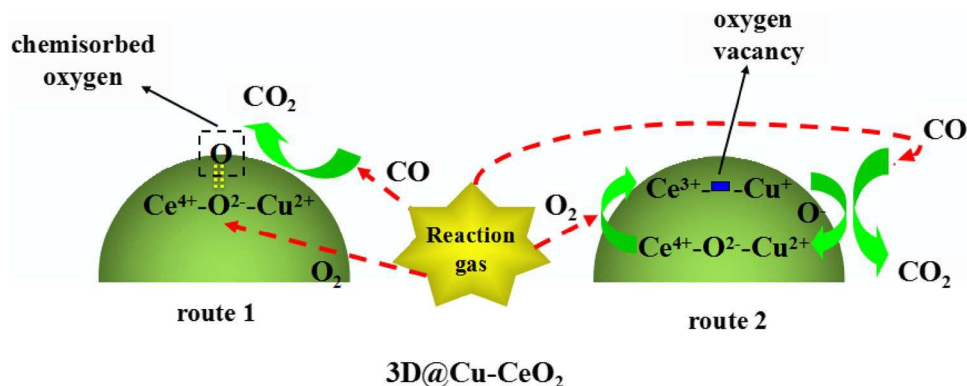
3.6 Reaction Mechanism Speculate

Based on the experimental results, a possible reaction mechanism with two reaction routes for CO catalytic oxidation over 3D@Cu–CeO₂ was proposed (Fig. 10). In the route 1, chemisorbed oxygen on the catalyst surface directly reacted with CO and the CO was oxidized into CO₂. The O₂ of reaction gas will form new chemisorbed oxygen. The reaction process will continue by this reaction mechanism. The route 2, the active lattice oxygen of catalyst react with CO and CO was oxidized into CO₂, meanwhile the catalyst produced the oxygen vacancy, which would be replenished by O₂ of reaction gas to form the new active lattice oxygen. The reaction process will continue by this reaction mechanism.

4 Conclusion

The 3D@Cu–CeO₂ and 2D@Cu–CeO₂ were successfully prepared by using hard template method, and the nano@Cu–CeO₂ was synthesized by the precipitation reaction. By comparing with 2D@Cu–CeO₂ and nano@Cu–CeO₂, the 3D@Cu–CeO₂ exhibited the best CO catalytic activity, with T₁₀₀ of 50 °C, and T₅₀ as low as 34 °C. According to the experimental results, we propose that the high activity is attributed to large lattice defect and oxygen vacancy resulted from a larger specific surface area and three-dimensional channel structure of the 3D@Cu–CeO₂

Fig. 10 Proposed CO reaction pathways over the catalysts: 3D@Cu–CeO₂



catalyst. The lattice defect and oxygen vacancy facilitates the activation of oxygen in the gas and the formation of active chemisorbed oxygen onto the catalyst surface. The active oxygen species played a crucial role in CO oxidation reaction for the 3D@Cu–CeO₂ catalyst. In addition, the 3D@Cu–CeO₂ catalyst exhibited high stability for CO catalytic oxidation, indicating it possesses potential non-noble catalyst in practical application. Our 3D@Cu–CeO₂ catalyst provides an excellent candidate for CO oxidation with activity higher than other reported similar catalysts.

Acknowledgments Wenzhou government's startup fund (WIBEZD2014004-02), The financial support of The National Basic Research Program of China (2013CB933201), the National Natural Science Foundation of China (21375125, 201605116), the Creative Research Group Project of National Natural Science Foundation of China (21321064) are gratefully acknowledged.

References

- Na H, Zhu T, Liu Z (2014) *Catal Sci Technol* 4:2051
- Su YF, Tang ZC, Han WL, Song Y, Lu GX (2015) *Catal Surv Asia* 19:68
- Feng Y, Zheng X (2010) *Nano Lett* 10:4762
- Socaciu LD, Hagen J, Bernhardt TM, Wöste L, Heiz U, Häkkinen H Landman U (2003) *J Am Chem Soc* 125:10437
- Hagen J, Socaciu LD, Elizajfer M, Heiz U, Bernhardt TM, Wöste L (2002) *Phys Chem Chem Phys* 4:1707
- Jena NK, K.R.S. Chandrakumar, Ghosh SK (2012) *J Phys Chem C* 116:17063
- Kang Y, Sun M, Li A (2012) *Catal Lett* 142:1498
- Wong K, Zeng QH, Yu AB (2011) *Chem Eng J* 174:408
- Kim SH, Jung CH, Sahu N, Park D, Yun JY, Ha H, Park JY (2013) *Appl Catal A Gen* 454:53
- Han WL, Zhang GD, Zhao K, Lu GX, Tang ZC (2015) *Phys Chem Chem Phys* 17:29027
- Su YF, Tang ZC, Song Y, Han WL, Zhang P (2014) *Cryst Eng Comm* 16:5189
- Li WL, Ge QJ, Ma XG, Chen YX, Zhu MZ, Xu HY, Jin RC (2016) *Nanoscale* 8:2378
- Liotta LF, Di Carlo G, Longo A, Pantaleo G, Venezia AM (2008) *Catal Today* 139:174
- Sun SS, Mao DS, Yu J, Yang ZQ, Lu GZ, Ma Z (2015) *Catal Sci Technol* 5:3166
- Teng ML, Luo LT, Yang XM (2009) *Micropor Mesopor Mater* 119:158
- Su YF, Tang ZC, Han WL, Song Y, Lu GX (2015) *Catal Surv Asia* 19:129
- Zou GC, Xu Y, Wang SJ, Chen MX, Shangguan WF (2015) *Catal Sci Technol* 5:1084
- Chagas CA, Souza EF, Manfro RL, Landi SM, Souza MMVM, Schmal M (2016) *Appl Catal B Environ* 182:257
- Li JF, Lu GZ, Li HF, Wang YQ, Guo Y, Guo YL (2011) *J Colloid Interf Sci* 360:93
- Soykal II, Sohn H, Ozkan US (2012) *ACS Catal* 2:2335
- Rao RC, Yang M, Li CS, Dong HZ, Fang S, Zhang AM (2015) *J Mater Chem A* 3:782
- Ren Y, Ma Z, Bruce PG (2012) *Chem Soc Rev* 41:4909
- Yen H, Seo Y, Kaliaguine S, Kleitz F (2012) *Angew Chem Int Ed* 51:12032
- Chen GZ, Xu QH, Yang Y, Li CC, Huang TZ, Sun GX, Zhang SX, Ma DL, Li X (2015) *ACS Appl Mater Interfaces* 7:23538
- Wei CH, Zhang XL, Lu LL, Song YY, Sun ZB (2015) *J Mater Sci Chem Eng* 3:154
- Li SL, Wang NL, Yue YH, Wang GS, Zu Z, Zhang Y (2015) *Chem Sci* 6:2495
- Kleitz F, Choi SH, Ryoo R (2003) *Chem Commun* 17:2136
- Zhao DY, Feng JL, Huo QS, Melosh N, Fredrickson GH, Chmelka BF, Stucky GD (1998) *Science* 279:548
- Li JJ, Ma CY, Xu XY, Yu JJ, Hao ZP, Qiao SZ (2008) *Environ Sci Technol* 42:8947
- Qu ZP, Yu FL, Zhang XD, Wang Y, Gao JS (2013) *Chem Eng J* 229:522
- Jiao F, Jumas JC, Womes M, Chadwick AV, Harrison A, Bruce PG (2006) *J Am Chem Soc* 128:12905
- Ji PF, Zhang JL, Chen F, Anpo M (2008) *J Phys Chem C* 112:17809
- Díaz G, Pérez-Hernández R, Gómez-Cortés A, Benaissa M, Mariscal R, Fierro JLG (1999) *J Catal* 187:1
- Henderson MA, Perkins CL, Engelhard MH, Thevuthasan S, Peden CHF (2003) *Surf Sci* 526:1
- Wang YG, Wang F, Chen YT, Zhang DF, Li B, Kang SF, Li X, Cui LF (2014) *Appl Catal B Environ* 147:602
- Wu ZL, Li MJ, Howe J, Meyer HM, Overbury SH (2010) *Langmuir* 26:16595
- Xu DY, Cheng F, Lu QZ, Dai P (2014) *Ind Eng Chem Res* 53:2625
- Barbero BP, Gamboa JA, Cadús LE (2006) *Appl Catal B Environ* 65:21
- Xue L, Zhang CB, He H, Teraoka Y (2007) *Appl Catal B Environ* 75:167
- Bai BY, Arandiyani H, Li JH (2013) *Appl Catal B Environ* 142–143:677

41. Jia AP, Jiang SY, Lu JQ, Luo MF (2010) *J Phys Chem C* 114:21650
42. Luo MF, Ma JM, Lu JQ, Song YP, Wang YJ (2007) *J Catal* 246:52
43. Mai HL, Zhang DS, Shi LY, Yan TT, Li HR (2011) *Appl Surf Sci* 257:7551
44. Cui XZ, Wang YX, Chen LS, Shi JL (2014) *ChemCatChem* 6:2860